SSRG International Journal of Electronics and Communication Engineering
ISSN: 2348-8549/ https://doi.org/10.14445/23488549/IJECE-V11I5P106

Volume 11 Issue 5, 59-68, May 2024
© 2024 Seventh Sense Research Group®

Original Article

Collaborative Filter Paradigm to Remove Noise in MRI Modality: Application to Diffusion Weighted Images

Anjanappa.C[1*], Puneeth S[1], Vishwanath M K[1], Rashmi S N[2], Madan Kumar L[3], B Hulugappa[4]

[1]*Department of Electronics and Communication Engineering, The National Institute of Engineering, Karnataka, India.*
[2]*Department of Industrial and Production Engineering, The National Institute of Engineering, Karnataka, India.*
[3]*Department of Civil Engineering, The National Institute of Engineering, Karnataka, India.*
[4]*Department of Mechanical Engineering, The National Institute of Engineering, Karnataka, India.*

[*]*Corresponding Author : anjanappagayathri@gmail.com*

Received: 12 March 2024 Revised: 21 April 2024 Accepted: 09 May 2024 Published: 31 May 2024

Abstract *- Denoising volumetric data is essential for improving data quality and facilitating accurate analysis, interpretation, and diagnostic capabilities in various fields, including medical imaging, scientific visualization, and engineering simulations. This article proposes a BM4D, an expansion of the BM3D filter designed specifically for volumetric data. This unique approach combines grouping and Collaborative Filtering (CF) principles. It entails grouping dimensionally similar patches into a (d + 1)-dimensional array, then processing them collectively in the transform domain. Unlike BM3D, where basic data patches are pixel blocks, BM4D uses voxel cubes combined into a Four-Dimensional (4-D) "Group." This 4-D transformation takes advantage of local correlations inside each voxel cube as well as non-local correlations between matching voxels from other cubes. This produces a highly sparse spectrum within this group, allowing for effective signal-to-noise distinction via coefficient reduction. Estimates for each grouped cube are received after applying the inverse transformation, which is then adaptively mixed at their original positions. The proposed algorithm's performance is assessed in the context of denoising volumetric data corrupted by Gaussian and Rician noise. Experimental results showcase BM4D's outstanding denoising capabilities, establishing its effectiveness in the domain of volumetric data denoising and positioning it as a cutting-edge solution.*

Keywords *- Collaborative filter, Block matching (BM4D), Diffusion Weighted Images (DWI), Tractography, Orientation Distribution Function (ODF), Volumetric data denoising.*

1. Introduction

Magnetic Resonance Imaging (MRI) scans are susceptible to various factors that can degrade the image quality and introduce unwanted artifacts into the original signal. Among these, noise is the most noticeable degrading element. Noise in MR scans is generally caused by two sources: thermal noise produced by the individual or object getting imaged and electrical noise produced during the acquisition of signals in the receiver chain. This noise is inherently intertwined with the MRI acquisition process and is, therefore, an inevitable part of the imaging procedure. Certain modern MRI acquisition sequences are particularly susceptible to the detrimental effects of noise. For instance, sequences in which the signal is attenuated, such as diffusion sequences with high b-values, tend to be significantly impacted by noise. This is also the case for techniques that require a substantial amount of data to be gathered in a shorter time frame, leading to a reduction in the Number of Excitations (NEX). Consequently, as the NEX decreases, the power of noise increases proportionally, following the square root of the speedup factor. The impact of noise-induced degradation in quality can have adverse consequences on the clarity of visual images, potentially impeding the accurate interpretation and analysis of data. Noise does not solely compromise visual assessment but also hampers various routine post-processing tasks such as tissue segmentation, image registration, and diffusion tensor estimation, as well as the precise acquisition of measurements and quantitative biomarkers in imaging. One direct method to mitigate the noise's effect on the ultimate image is to employ noise reduction techniques, alternatively referred to as denoising or, from a statistical viewpoint, signal estimation.

Noise reduction methods in medical imaging have historically made use of preexisting statistical models of data, with the Gaussian distribution being a common assumption in many algorithms. These methods have progressed to accommodate the particularities of MRI data as more sophisticated noise models for MRI have been developed. Numerous examples, such as the Conventional Approach (CA), linear estimators, Maximum Likelihood (ML), and modified Non-Local Mean (NLM) methods, may be found in the current literature [1–18]. Single-coil acquisitions present the simplest case, and the complicated spatial MR data is usually represented as a complex Gaussian process. It is

This is an open access article under the CC BY-NC-ND license (http://creativecommons.org/licenses/by-nc-nd/4.0/)

assumed that the original signal's real and imaginary parts are both contaminated by independent Gaussian noise with a mean of zero and a uniform variance of σ^2. For this reason, a Rician distribution [19] holds for the magnitude signal, which is produced by computing the envelope of the complex signal. For many years, this Rician model has been used as the gold standard in MRI modeling, and it has served as the foundation for numerous filtering methods and noise estimation algorithms [20].

2. Materials

Data was gathered from two distinct sources: a brain-simulated database [26] and the OASIS dataset. The former comprises structural MR data, while the latter contains nonstructural MRI data [21-24]. The structural MRI data, taken from a horizontal view with a slice number of 91, had imaging parameters as follows: TR (Repetition Time) of 9.7 milliseconds, TE (Echo Time) of 4.0 milliseconds, a flip angle of 10 degrees, a voxel dimension of 256x256x128, and a resolution of 1.0x1.0x1.25 millimeters. The second dataset, involving nonstructural MRI, featured specific imaging parameters, including 15 diffusion directions with b-values of 1000s/mm2 and 2000s/mm2, as well as a b-value of 3000s/mm2. The volume had TR/TE values of 17,000/80 milliseconds, a resolution of 1.5x1.5x1.5 mm3, a volume size of 148x148x90, and a NEX (Number of Excitations) value of 1.

3. Method

The BM3D image denoising method [18] exemplifies the concept of grouping and CF, which is an important extension of the non-local filtering technique. The transform domain sparse representation is the foundation of this approach. To improve sparsity, related 2-D image pieces are gathered into 3-D data arrays known as groups. CF is a particular process that these communities go through. It consists of three phases. The first step is to translate the group into 3-D. The second change is a decrease in the size of the modified group's coefficients. As a last step, the 3-D transformation is inverted to derive the 3-D group estimate. The noise is efficiently segregated throughout the shrinking phase because of the commonalities between the grouped fragments. This is made possible by the 3-D transformation, which, in the transform domain, reveals a highly sparse representation of the authentic signal. As a result, CF not only brings out the tiniest details shared by the collaboratively filtered 2-D fragments but also keeps their personalities intact.

The BM3D algorithm, as introduced in reference [18], is the leading technique in the realm of 2-D image denoising, showcasing markedly better performance compared to all earlier approaches. Recent research has explored the near-optimality of this approach, shedding light on its fundamental principles. In this research, BM4D is introduced as a refinement of the BM3D method, tailored specifically for denoising volumetric data. The suggested BM4D technique naturally uses voxel cubes as its core units, whereas BM3D works with basic data patches made of pixel blocks. The creation of an arrangement by stacking identical cubes on top of one another results in the formation of a 4-D orthotope, also referred to as a hyperrectangle. In this hyperrectangle, the fourth dimension represents the stacking direction of the cubes, signifying non-local correlations present within the data.

Consequently, CF functions on harnessing both the local correlations within each cube's voxels and the non-local correlations among corresponding voxels in different cubes. Much like the approach employed in BM3D, this group's spectral characteristics demonstrate significant sparsity, making it highly effective for distinguishing between signal and noise through methods such as thresholding or Wiener Filter (WF). Following an inverse transformation, estimations for each grouped cube are obtained, and these estimations are then merged at their original positions with the application of adaptive weights.

3.1. Noise Model

Consider the noisy volumetric observation $z: X \rightarrow R$

$$z(x) = y(x) + \eta(x),\ x \epsilon X \tag{1}$$

Where $\eta(x)$ represents Gaussian noise in the data, which has independent and identically distributed features with zero mean and an established Standard Deviation (SD), σ. y represents the original, unidentified volumetric signal, and x represents a 3-D coordinate within the domain.

3.2. BM4D Algorithm

The main objective of the BM4D method being discussed is to produce an estimate, represented as $\hat{y}$, for the initial signal y, using the noisy input z. BM4D operates through a two-step procedure, comprising an initial Hard-thresholding phase, succeeded by a subsequent WF stage. Each of these stages holds three essentials: Grouping, collaborative filtering, and aggregation.

3.2.1. Hard-Thresholding Stage

The 4-D groups form by orienting themselves along an extra dimension, similar to how cubes coordinate within a reference cube. The photometric distance is employed to compare the similarities of the two cubes.

$$d\left(C^z_{x_i}, C^z_{x_j}\right) = \frac{||C^z_{x_i} - C^z_{x_j}||_2^2}{L^3} \tag{2}$$

Here, $||.||_2^2$ is the total squared dissimilarities between pairs of input cubes' intensity values. Extracted from z at the top-left-front 3D position $x_R \in X$, $C^z_{x_R}$ is a cube of $L \times L \times L$ voxels, $L \in N$. L^3 is a normalizing denominator, where L is the length of a cube.

3.2.2. Grouping Step

The value sets the lowest level of acceptable cube-similarity τ_{match}^{ht}, which determines whether or not two cubes are considered similar based on the equation above. The process commences with the definition of a set. $S_{x_R}^{\hat{y}^{ht}}$ That includes the indices of all the cubes that are close to the reference cube. $C_{x_R}^{z}$. Using such a set, one may construct the 4-D group. $G_{S_{x_R}^{z}}^{z}$.

$$\text{Set:} \quad S_{x_R}^{\hat{y}^{ht}} = \{ x_i \in X : \ d\left(C_{x_R}^{z}, C_{x_i}^{z} \right) < \tau_{match}^{ht} \} \qquad (3)$$

$$\text{Group:} \quad G_{S_{x_R}^{z}}^{z} = \coprod_{x_i \in S_{x_R}^{z}} C_{x_i}^{z} \qquad (4)$$

3.2.3. Collaborative Filtering Step

A combined 4-D transformation, represented as four distinct 1-D decor-related linear transformations, denoted as T_{4D}^{ht}, is individually applied to each dimension within the group. The resulting 4-D group spectrum is subsequently subjected to coefficient-by-coefficient reduction using a hard-thresholding operator denoted as γ^{ht}, with a threshold value defined as $\gamma^{ht}(\mathrm{T}_{4D}^{ht}(G_{S_{x_R}^{z}}^{z})$. The filtered group is generated by performing an inversion of the 4-D transform, as specified in the following definition.

$$\mathrm{T}_{4D}^{ht\,-1}(\gamma^{ht}(\mathrm{T}_{4D}^{ht}(G_{S_{x_R}^{z}}^{z}))) = \widehat{G_{S_{x_R}^{z}}^{y}} = \coprod_{x_i \in S_{x_R}^{z}} \widehat{C_{x_\iota}^{z}} \qquad (5)$$

Each $\widehat{C_{x_\iota}^{z}}$ represents a prediction of the original $C_{x_i}^{y}$, which is derived from the unknown volumetric data y.

3.2.4. Aggregation Step

The CF process leverages the redundancy within it by employing an adaptive convex combination, yielding the fundamental volumetric prediction.

$$\widehat{y^{ht}} = \frac{\Sigma_{x_R \in X}(\Sigma_{x_i \in S_{x_R}^{z}} w_{x_R}^{ht} \widehat{C_{x_\iota}^{y}})}{\Sigma_{x_R \in X}(\Sigma_{x_i \in S_{x_R}^{z}} w_{x_R}^{ht} \widehat{\chi_{x_\iota}})} \qquad (6)$$

In this case, $w_{x_R}^{ht}$ denotes group-specific weights, and $\widehat{\chi_{x_\iota}}$: X →{0, 1} denotes a characteristic (indicator) function for the domain of $\widehat{C_{x_\iota}^{y}}$. This function has a value of one over the coordinates of the voxels of $\widehat{C_{x_\iota}^{y}}$ and a value of zero elsewhere. It is vital to note that outside of its domain, every $\widehat{C_{x_\iota}^{y}}$ is presumed to be zero-padded. The weights are defined as

$$w_{x_R}^{ht} = \frac{1}{\sigma^2 N_{x_R}^{ht}} \qquad (7)$$

Where σ is the SD of the noise in z and $N_{x_R}^{ht}$ the content represents the count of non-zero coefficients within the group spectrum. Groups that display a strong correlation receive increased weighting, while those with significant residual noise receive reduced weighting as a penalty.

3.2.5. Wiener Filtering Stage

The grouping is done inside the fundamental estimate. $\hat{y}^{ht}$ produced in the previous phase of hard thresholding. Anticipated outcomes include achieving enhanced precision and dependability in matching due to the substantially lower level of noise in the primary estimate compared to that in "z." This improved grouping will, in turn, facilitate a more efficient reduction of the group spectrum's complexity, ultimately yielding a superior quality of noise reduction. A collection of coordinates for similar cubes is assembled for each reference cube, $C_{x_R}^{\hat{y}^{ht}}, they\,are$ retrieved from the original estimate.

$$S_{x_R}^{\hat{y}^{ht}} = \{ x_i \in X : d\left(C_{x_R}^{\hat{y}^{ht}}, C_{x_i}^{\hat{y}^{ht}} \right) < \tau_{match}^{wie} \} \qquad (8)$$

Where d (.) is defined in equation (2) and τ_{match}^{wie} is the predefined threshold value of the WF stage. CF is employed in the form of an empirical WF. Initially, a subset is derived from the fundamental estimation based on the provided coordinates. Subsequently, the coefficients of the empirical WF are determined by considering the energy of its spectrum.

$$W_{S_{x_R}^{\hat{y}^{ht}}} = \frac{|\mathrm{T}_{4D}^{wie}(G_{S_{x_R}^{\hat{y}^{ht}}}^{\hat{y}^{ht}})|^2}{|\mathrm{T}_{4D}^{wie}(G_{S_{x_R}^{\hat{y}^{ht}}}^{\hat{y}^{ht}})|^2 + \sigma^2} \qquad (9)$$

The 4D transform operator, T_{4D}^{wie}, consists of four 1-D linear transformations that differ from those found in the hard thresholding filter. $G_{S_{x_R}^{\hat{y}^{ht}}}^{z}$ is a noisy group created by using the set from equation (8). The WF coefficients are multiplied by the noisy group's spectral elements to reduce the size of the coefficients. The group's estimate is provided by

$$\widehat{G_{S_{x_R}^{\hat{y}^{ht}}}^{y}} = \mathrm{T}_{4D}^{wie\,-1}(W_{S_{x_R}^{\hat{y}^{ht}}} . \mathrm{T}_{4D}^{wie}(G_{S_{x_R}^{\hat{y}^{ht}}}^{z})) \qquad (10)$$

Where $\mathrm{T}_{4D}^{wie}\left(G_{S_{x_R}^{\hat{y}^{ht}}}^{z} \right)$ represents the noisy group spectrum. The group estimate is generated by performing a reverse 4-D transformation on the compressed spectrum. The total weights for a particular group estimate (designated as 11) are determined based on the WF coefficient's energy.

$$w_{x_R}^{wie} = \sigma^{-2} ||W_{S_{x_R}^{\hat{y}^{ht}}}||_2^{-2} \qquad (11)$$

4. Results

The experiments involve conducting tests with two types of noise distributions: Gaussian and Rician. When considering the Gaussian distribution, the observations z, which are affected by noise, follow the distribution described in Equation (1). The noisy observations z: $X \rightarrow R^+$, in the case of Rician distributed noise, obey the definition.

$$z(x) = \sqrt{(c_r.y(x) + \sigma_r.\eta_r(x))^2 + (c_i.y(x) + \sigma_i.\eta_i(x))^2} \quad (12)$$

Here, x is a 3-D position within the X domain (a subset of Z^3), and $c_r$and c_i are constants meeting the criteria $0 \leq c_r,c_i \leq 1 = {c_r}^2 + {c_i}^2$. Furthermore, $\eta_r(.)$ and $\eta_i(.)$ are random vectors with a normal distribution. This arrangement yields $z \sim R(y,\sigma)$, which represents the unprocessed MR data as a Rician distribution with parameters y and σ. In this case, y denotes the underlying noise-free signal, which is unknown, and σ indicates the Rician noise SD.

To effectively apply the BM4D algorithm to Rician noise-affected data, a technique known as Variance Stabilization Transformation (VST) is employed, as detailed in reference [25]. Before beginning with the denoising procedure, the fundamental goal of VST is to break the link between noise variance and the underlying signal. Furthermore, it attempts to mitigate the effect of bias in the resultant filtered estimation. Denoising Rician data with the BM4D technique might be expressed in formal terms as follows:

$$\hat{y} = VST^{-1}(\text{BM4D (VST (z,}\sigma),\sigma_{VST}),\sigma) \quad (13)$$

Where $\sigma_{VST}$is the stabilized SD produced by the VST. Table 1 lists recommended parameter combinations for optimizing the performance of the BM4D algorithm. These options are divided into two categories: "normal" and "modified." The typical profile strikes a decent balance between computational complexity and denoising efficacy. The updated profile, on the other hand, prioritizes minimizing computational complexity, although at the expense of diminished denoising performance.

Several parameters in the updated profile are changed, including the similarity threshold (τ), cube size (L), group size (M), and hard-threshold value (λ_{4D}). T_{4D}^{ht} is a composite transformation that combines a 3-D biorthogonal spline wavelet and a 1-D Haar Wavelet (1-DHW). T_{4D}^{wie} incorporates a 3-D Discrete Cosine Transform with a 1-DHW during the WF stage. It is critical to note that there is no prefiltering before the cube-matching stage, which means that noisy data are evaluated for similarity immediately. The denoised signal is represented more completely than necessary by the hard thresholding groups. This is because cubes from different and same groups can overlap, leading to multiple, and often conflicting, voxel estimations in the overlapping regions. The cubes are grouped according to their coordinates inside a three-dimensional window of size $Ns * Ns * Ns$, where Ns is the size of the cube being searched. Nstep separates the reference cubes in every spatial dimension. If noise variance is high (σ> 15%), the revised profile delivers the best PSNR efficiency constantly.

Low-frequency elements, a wide variety of related patches, and a homogenous background differentiate the Brain Web phantom. The new strategy takes advantage of these characteristics in two ways: it creates larger groups while applying more aggressive smoothing via a higher hard threshold value. Non-local cube-matching searches take the longest and are mostly governed by variables such as the 3-D search window's size (Ns) and the step between processed cubes ($Nstep$). In the current execution, the only rapid approach is the 1-D transformation done to the 4-D (grouping), but the 3-D separable modification for every cube will be performed via matrix multiplications. As a result, to accelerate BM4D, quick transformation techniques on the cube dimensions might be used. Table 2 gives the PSNR and execution times for BM4D with various Ns and $Nstep$ combinations; however, when $Ns > 3$ and $Nstep \leq L$, optimal filtering results are obtained to optimize grouping and prevent potential missing estimations in the final denoised volume.

Table 1. BM4D algorithm parameter settings for structural and DWI Data

Parameter		Stage			
		Hard Thresholding		WF	
		Normal	Modified	Normal	Modified
Group Size	**M**	16	32	32	
Cube Size	**L**	4	4	5	
Search-Cube Size	**N_S**	11			
Step	**N_{step}**	3			
Shrinkage Threshold	**λ_{4D}**	2.7	2.8	Does not apply	
Similarity Threshold	**Γmatch**	2.9	24.6	0.4	6.7

The PSNR of the denoising is used to assess its objective quality.

$$\text{PSNR}(y,\hat{y}) = 10\ log_{10}\left(\frac{D^2|\hat{X}|}{\sum_{x \in \hat{X}}(\hat{y}(x)-y(x))^2}\right) \quad (14)$$

These experiments are assessed using the y peak, labeled as D, and y as a representation of y." Additionally, also employed the Structural Similarity Index (SSIM) to evaluate the experiments. While originally designed for 2-D data, SSIM has been extended to accommodate 3-D data as well. SSIM provides greater alignment with the human visual system than traditional approaches based on mean squared error, such as PSNR. The output of the denoising algorithm taking Brain-Web phantom as input and at σ value of 7% Gaussian noise and ricin is given below. In this case, the input image is cropped so that a specific portion of the image is denoised to reduce time consumption. The following Figure 1 is the output of the same input without cropping the image (the entire image is denoised). The PSNR value and SSIM value change from cropped input, but the change is of very little value. Table 3 PSNR and SSIM [27] metrics are employed to evaluate the denoising performance of the suggested BM4D approach. This analysis is based on the Brainweb database [26]. Two types of observations are investigated, one of which is deliberately contaminated with homogenous Rician noise by certain observation models. These observations are checked at various SDs, which are reported as a percentage of the greatest intensity value in the original data. A VST built for Rician-distributed data is used in the evaluation [25].

Table 2. BM4D's denoising performance in terms of execution time with matching parameters

Parameters		SD of Noise (σ)				Execution Time
Ns	**N_{step}**	**7%**	**11%**	**15%**	**19%**	**(in Seconds)**
1	5	28.67	26.78	24.23	22.21	5
	4	31.23	26.66	25.11	22.44	8
	3	33.99	26.55	25.22	22.77	10
3	5	35.87	34.44	32.21	31.11	50
	4	36.67	34.55	33.55	31.44	90
	3	36.56	34.67	33.66	31.55	150
5	5	36.76	34.23	33.23	31.89	250
	4	35.44	34.88	34.23	31.98	310
	3	34.78	34.86	34.55	31.97	450
7	5	37.21	35.34	34.45	33.34	455
	4	37.23	35.44	35.55	33.44	345
	3	38.00	35.33	35.66	33.55	125
9	5	38.26	37.34	36.55	35.23	145
	4	38.82	36.66	36.66	36.66	234
	3	39.09	37.35	36.88	36.88	444
11	5	40.11	38.55	37.34	36.34	312
	4	40.45	38.66	37.36	36.89	245
	3	40.55	38.77	37.66	36.91	234
13	5	41.23	39.11	38.34	37.23	566
	4	41.66	38.22	38.22	37.45	255
	3	41.22	38.33	38.55	37.55	666
15	5	42.11	40.89	39.89	38.23	435
	4	42.55	40.91	39.91	38.67	255
	3	42.77	40.98	39.93	38.68	899

Table 3. PSNR and SSIM metrics

Noise	Filter	SD of Noise (σ)							
		1%	**3%**	**5%**	**9%**	**11%**	**15%**	**17%**	**19%**
Rician Noise	Noisy Data	40.00|0.97	35.33|0.86	31.67|0.78	28.66|0.65	25.22|0.55	21.00|0.34	17.54|0.25	12.11|0.15
	NLM 3D	43.22|0.99	41.56|0.97	38.54|0.95	36.78|0.91	35.91|0.89	34.98|0.87	33.34|0.85	31.76|0.77
	LMMSE 3D	44.45|0.99	43.45|0.95	42.21|0.81	39.98|0.79	37.22|0.86	35.23|0.77	31.23|0.69	28.99|0.55
	Proposed Filter	45.25|0.99	41.89|0.94	38.22|0.86	36.66|0.77	34.11|0.66	32.21|0.55	30.99|0.45	29.98|0.33

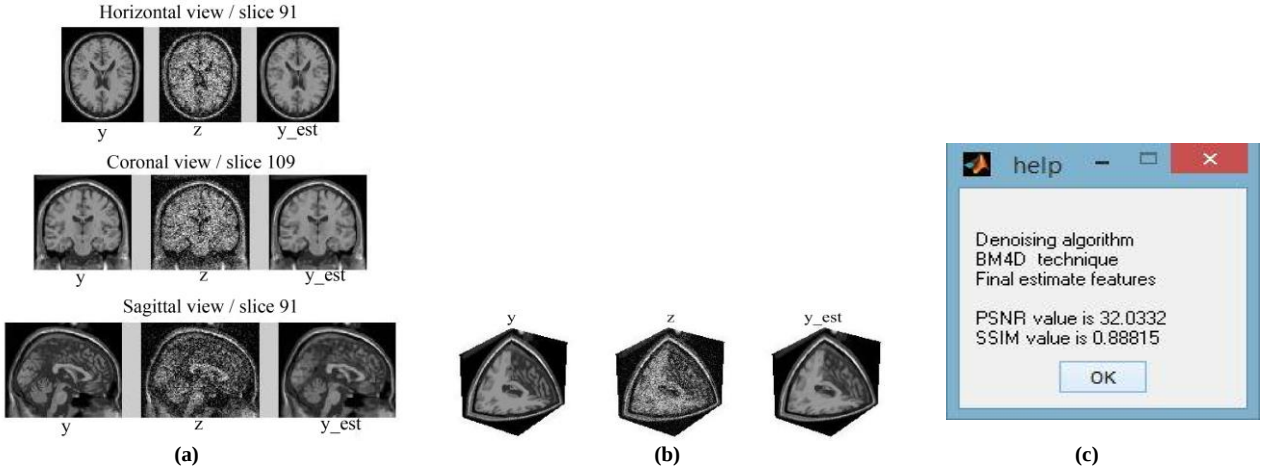

(a) **(b)** **(c)**

Fig. 1(a) Uncropped phantom denoising output, (b) Uncropped phantom denoising output views, and (c) Output dialogue box.

4.1. Application to Volumetric Data Denoising in DWI Images

Volumetric Data Denoising in DWI images plays a pivotal role in neuroimaging, enabling the visualization of microscopic tissue structures and connectivity within the brain. However, DWI images are inherently noisy due to factors like physiological motion, hardware imperfections, and low Signal-to-Noise Ratio (SNR). Denoising these images is crucial for accurate analysis and interpretation. Figure 2 shows the flow chart of the suggested Collaborative BM4D technique Applied to DWI Images.

4.2. Comparison Results Using Simulation Data

A comparative analysis was conducted between the proposed BM4D algorithm and a traditional filter using simulated DW data corrupted by Rician noise. BM4D was configured with a specific set of parameters outlined in Table 1. In Figure 3, A quantitative assessment of DW data denoised by three distinct approaches was presented, considering various noise levels ranging from 0.01 to 0.1, with increments of 0.01. across all four quantitative parameters, BM4D regularly outperforms the other methods. To be more exact, the PSNR of BM4D is roughly 14% higher than that of NLM and approximately 5% higher than that of LMMSE and Joint Local Mean-Mean Squared Error (JLMMSE). Comparison with the NLM method, the FA-RMSE, MD-RMSE, and Tensor-Fro. dist of BM4D exhibit 40%, 48%, and 37% reductions, correspondingly. Figure 4 depicts denoised DWI at b=2000 s/mm2 for one representative encoding direction, along with fitted and color-coded Fractional Anisotropy (FA) maps and its related error mappings under Rician noise with n = 0.05. All approaches perfectly decrease image noise. However, BM4D beats NLM and JLMMSE in terms of better detail preservation. The BM4D image looks similar to the actual images without noise, which is comparable with the measured PSNR estimate displayed in the figures. FA and color-coded FA maps created from BM4D images exhibit the strongest correlations with reference maps, surpassing NLM and JLMMSE maps. Figure 4 depicts the ODFs calculated from the data. ODFs from BM4D images are similar to actual images without noise than NLM and LMMSE. Figure 4 also shows a visual representation of the FA quantification errors for the NLM, LMMSE, and BM4D methods.

In comparison to NLM, the FA errors associated with LMMSE and BM4D are concentrated closer to zero, with reduced bias (dashed plot) and variance (solid plot). Significantly, BM4D denoised images exhibit a marginally reduced variance and bias in FA errors compared to LMMSE, thereby confirming the effective preservation of diffusion tensor anisotropy by BM4D denoised images. Figure 4 compares three methods that employed the same initial brain dataset with different b-values (1000, 2000, and 3000 s/mm2). Images having unique b-scores and gradient orientations were processed individually in the NLM technique execution, whereas images with all b- b-scores and gradient orientations were processed parallelly in the BM4D technique design. To ensure a fair comparison, the NLM, JLMMSE, and Joint Anisotropic Local Mean-Mean Squared Error (JALMMSE) techniques were applied to denoise the DWI on a per-coil basis, and the outcome was achieved by applying a sum-of-squares functioning to the denoised coil images.

Figure 4 shows the denoised images and their associated image residuals, along with FA and color-coded FA maps. Noise significantly degrades the original image's essential structures, especially with high b-values. All three methods reduced noise successfully; however, BM4D produced images with more distinct details and less residual noise than NLM and Linear Minimum Mean Squared Error (LMMSE). LMMSE and BM4D picture residuals contain anatomical information. The BM4D and LMMSE algorithms were employed on excellent spatial resolution DWI. The FA maps from the LMMSE and BM4D photographs are less noisy and closer to the reference images. Furthermore, as seen in Figure 4 and stated in Table 4, both LMMSE and BM4D restore the original ODFs in many locations, whereas NLM causes swelling and alters diffusion orientations in various places.

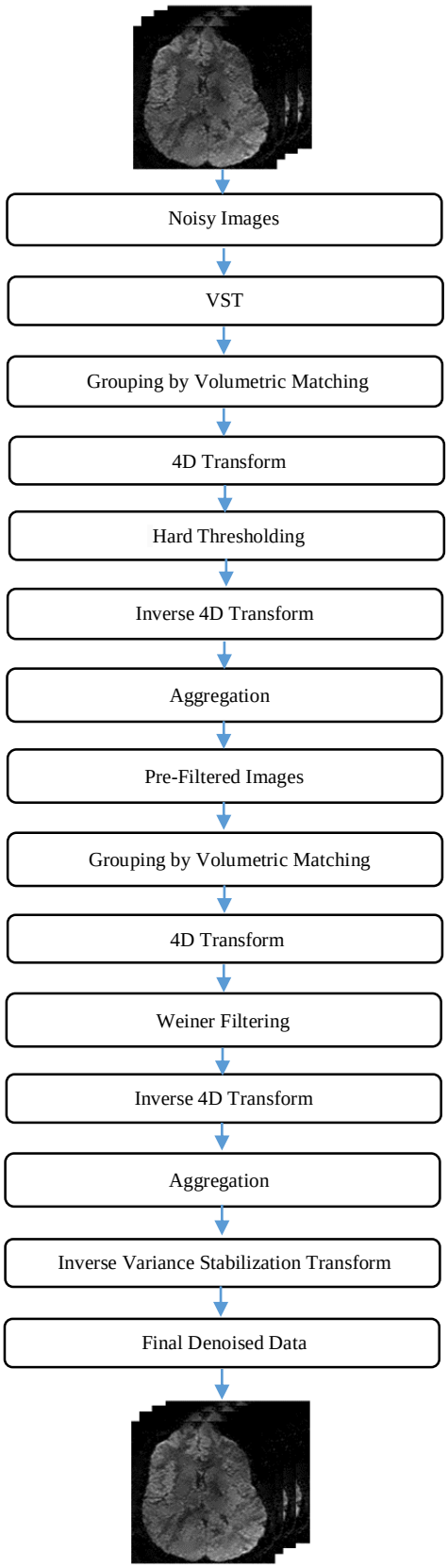

Fig. 2 Flow chart of the suggested collaborative BM4D technique applied to DWI images

A comparison with BM3D was undertaken to evaluate the BM4D algorithm's utility in improving the quality of volumetric DW data obtained from many directions. In terms of noise reduction while keeping image information, both the BM3D and BM4D approaches performed admirably. Notably, when compared to the BM3D-treated images, images processed with BM4D showed greater visual appeal, with sharper edges, as shown in the regions covered by blue squares. Moreover, the fibers traced in the actual noisy data looked sparse and chaotic, while those formed from denoised data looked richer and more ordered.

4.3. Comparison Results by Employing Vivo Data

Red squares bordered the indicated region, and the fibers detected in the BM4D-processed images appeared marginally more precise and finer as compared to the BM3D-processed images. The evidence highlights the proposed filter's effectiveness in not only lowering noise efficiently but also retaining anatomical structures. In the context of denoising multi-shell volumetric DWI, it was discovered that simultaneously filtering multiple b-value images outperformed separately filtering each b-value image. The same approach was used to denoise in vivo data recorded with b-values of 1000, 2000, and 3000 s/mm2, as shown in Figure 4. The current BM4D implementation searches photos for volumetric cuboids at all b values. Because non-DWI has a greater Signal-to-Noise Ratio (SNR) and more identifiable features than DW photos, a similar cuboid search can be performed using solely non-DWI. In this investigation, upon examination of both approaches, it was found that they yielded equivalent denoising outcomes. Regarding computational efficiency, NLM denoised generated DWI with a 256x256 matrix size and 44 diffusion directions in around 1.5 minutes, while BM4D required 14 minutes. All techniques were run in MATLAB 7.12.0 as single-threaded processes on a Windows 7 PC. Notably, the BM4D stage was the time-consuming element of the process, and its efficiency may be improved by using parallel computing techniques.

5. Discussion

This work introduces a novel strategy for enhancing the quality of both structural and DWI data. The proposed method's performance is evaluated using both synthetic and real clinical data and comparisons with existing state-of-the-art methodologies. Despite its simple architecture, the proposed method outperforms previously proposed methods in DWI denoising and estimation of diffusion parameters. Using a volumetric collaborative filter paradigm, noise in multidirectional DWI data is effectively reduced. This noise reduction capability is linked to the significant local profile similarity, which enables us to describe diffusion profiles with a minimum number of components, allowing for the efficient removal of non-signal-related factors such as noise. Furthermore, this research shows that the proposed method not only minimizes image noise but also mitigates the bias imposed by the Rician nature of the noise.

As a result, the diffusion parameters of the acquired data more precisely reflect the tissue features rather than being distorted by noise, as indicated by the FA values in Figure 4. Notably, the decrease in parameter estimation error is consistent across all noise levels examined.

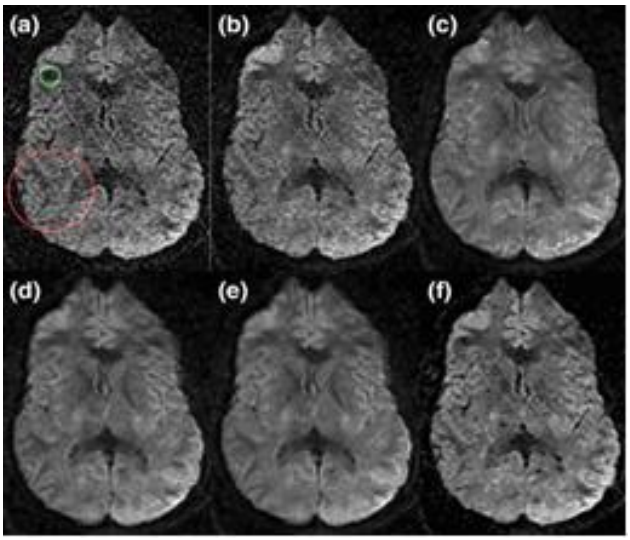

Fig. 3 Results of denoised filters (simulated data) a) Noisy image, b) NLM, c) LMMSE, d) JLMMSE, e) JaLMMSE, and f) Proposed filter.

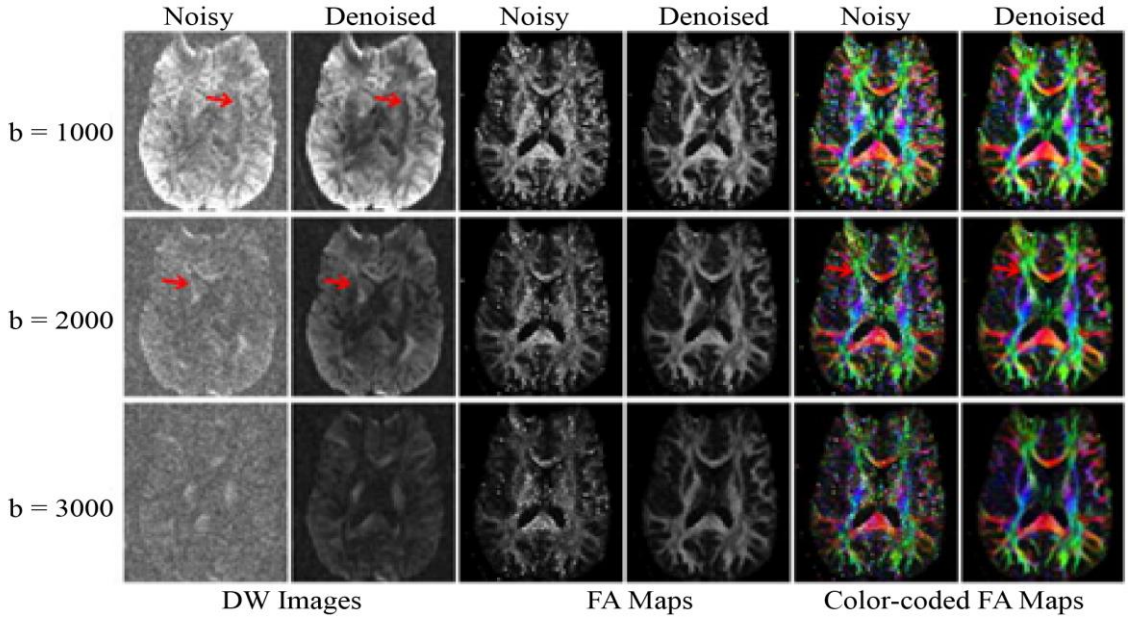

Fig. 4 Comparison between FA and color-coded FA map images derived from noisy DWI

Table 4. Comparison of PSNR metrics

Particulars	Volumetric DW01	Volumetric DW02	Volumetric DW03	Volumetric DW04	Volumetric DW05	Volumetric DW06	Volumetric Case Average
Case 1	46.41 39.87	44.41 37.66	43.36 36.88	41.55 36.11	40.48 38.88	39.91 37.66	39.68 37.76
Case 2	45.45 40.55	40.55 39.56	39.66 37.44	37.22 36.55	35.89 35.44	31.22 34.34	30.49 37.22
Volumetric Orientation Average	45.93 40.21	42.48 38.61	41.51 37.16	39.385 36.33	38.18 37.16	35.56 36.00	35.085 37.74

Furthermore, this denoised approach improved tractography results significantly. This resulted in a significant decrease in the uncertainty associated with nerve fiber orientation and an increase in the likelihood of connections between voxels along a given tract. As a result, tract construction became more reliable, examining tissue microstructure using tensor-derived metrics more sensitive. The quantitative diffusion maps created from simulated datasets demonstrated that reducing the influence of Rician noise on quantitative diffusion parameter estimation is most successful when DWI denoising is performed. Even when dealing with inhomogeneous noise, the BM4D technique outperformed algorithms such as JLMME and NLM.

The proposed method is easily adaptable to a wide range of multidirectional DWI datasets, regardless of the diffusion analysis method used, such as DTI, HARDI, q-ball, and others. This adaptability has the potential to improve the accuracy of quantitative metrics obtained from such datasets, providing immediate benefits for researching brain connections and tissue microstructure in both healthy and diseased brain situations.

6. Conclusion

In summary, this study illustrates the potential for enhancing the clarity of both structural and DW MR images through denoising. The results gathered from simulated and real-world data demonstrate this algorithm's usefulness in preserving precise information in DWI, reducing noise, and significantly improving the accuracy of following diffusion parameter measures. This approach is anticipated to advance the utilization of superior resolution and greater b-value DWI in future applications.

Funding Statement

The authors did not receive support from any organization for the submitted work. No funding was received to assist with the preparation of this manuscript. No funding was received for conducting this work.

References

[1] P. Perona, and J. Malik, "Scale-Space and Edge Detection Using Anisotropic Diffusion," *IEEE Transactions on Pattern Analysis and Machine Intelligence*, vol. 12, no. 7, pp. 629-639, 1990. [CrossRef] [Google Scholar] [Publisher Link]

[2] Yansun Xu et al., "Wavelet Transform Domain Filters: A Spatially Selective Noise Filtration Technique," *IEEE Transactions on Image Processing*, vol. 3, no. 6, pp. 747-758, 1994. [CrossRef] [Google Scholar] [Publisher Link]

[3] T. Aach, and D. Kunz, "Anisotropic Spectral Magnitude Estimation Filters for Noise Reduction and Image Enhancement," *Proceedings of 3rd IEEE International Conference on Image Processing*, Lausanne, Switzerland, vol. 1, pp. 335-338, 1996. [CrossRef] [Google Scholar] [Publisher Link]

[4] John C. Wood, and Kevin M. Johnson, "Wavelet Packet Denoising of Magnetic Resonance Images: Importance of Rician Noise at Low SNR," *Magnetic Resonance in Medicine*, vol. 41, no. 3, pp. 631-635, 1999. [CrossRef] [Google Scholar] [Publisher Link]

[5] R.D. Nowak, "Wavelet-Based Rician Noise Removal for Magnetic Resonance Imaging," *IEEE Transactions on Image Processing*, vol. 8, no. 10, pp. 1408-1419, 1999. [CrossRef] [Google Scholar] [Publisher Link]

[6] Leonid P. Yaroslavsky, Karen O. Egiazarian, and Jaakko T. Astola, "Transform Domain Image Restoration Methods: Review, Comparison, and Interpretation," *Proceedings of SPIE, Nonlinear Image Processing and Pattern Analysis XII*, vol. 4304, pp. 155-169, 2001. [CrossRef] [Google Scholar] [Publisher Link]

[7] Aleksandra Pizurica, "*Image Denoising Using Wavelets and Spatial Context Modeling*," Ph.D. Thesis, Ghent University, pp. 1-248, 2002. [Google Scholar] [Publisher Link]

[8] D.D. Muresan, and T.W. Parks, "Adaptive Principal Components and Image Denoising," *Proceedings 2003 International Conference on Image Processing*, Barcelona, Spain, pp. 1-101, 2003. [CrossRef] [Google Scholar] [Publisher Link]

[9] J. Sijbers, and A.J. Den Dekker, "Maximum Likelihood Estimation of Signal Amplitude and Noise Variance from MR Data," *Magnetic Resonance in Medicine*, vol. 51, no. 3, pp. 586-594, 2004. [CrossRef] [Google Scholar] [Publisher Link]

[10] Zhou Wang et al., "Image Quality Assessment: From Error Visibility to Structural Similarity," *IEEE Transactions on Image Processing*, vol. 13, no. 4, pp. 600-612, 2004. [CrossRef] [Google Scholar] [Publisher Link]

[11] R. Vincent, "*Brainweb: Simulated Brain Database*," McGill, 2006. [Google Scholar] [Publisher Link]

[12] Jan Sijbers et al., "Automatic Estimation of the Noise Variance from the Histogram of a Magnetic Resonance Image," *Physics in Medicine & Biology*, vol. 52, no. 5, 2007. [CrossRef] [Google Scholar] [Publisher Link]

[13] Kostadin Dabov et al., "Image Denoising by Sparse 3-D Transform-Domain Collaborative Filtering," *IEEE Transactions on Image Processing*, vol. 16, no. 8, pp. 2080-2095, 2007. [CrossRef] [Google Scholar] [Publisher Link]

[14] Santiago Aja-Fernandez et al., "Restoration of DWI Data Using a Rician LMMSE Estimator," *IEEE Transactions on Medical Imaging*, vol. 27, no. 10, pp. 1389-1403, 2008. [CrossRef] [Google Scholar] [Publisher Link]

[15] José V. Manjón et al., "MRI Denoising Using Non-Local Means," *Medical Image Analysis*, vol. 12, no. 4, pp. 514-523, 2008. [CrossRef] [Google Scholar] [Publisher Link]

[16] Karl Krissian, and Santiago Aja-Fernandez, "Noise-Driven Anisotropic Diffusion Filtering of MRI," *IEEE Transactions on Image Processing*, vol. 18, no. 10, pp. 2265-2274, 2009. [CrossRef] [Google Scholar] [Publisher Link]

[17] Alexander Wong, and Akshaya K. Mishra, "Quasi-Monte Carlo Estimation Approach for Denoising MRI Data Based on Regional Statistics," *IEEE Transactions on Biomedical Engineering*, vol. 58, no. 4, pp. 1076-1083, 2011. [CrossRef] [Google Scholar] [Publisher Link]

[18] Jeny Rajan et al., "An Adaptive Non Local Maximum Likelihood Estimation Method for Denoising Magnetic Resonance Images," *2012 9th IEEE International Symposium on Biomedical Imaging*, Barcelona, Spain, pp. 1136-1139, 2012. [CrossRef] [Google Scholar] [Publisher Link]

[19] P.V. Sudeep, P. Palanisamy, and Jeny Rajan, "A Hybrid Model for Rician Noise Reduction in MRI," *2013 2nd International Conference on Advanced Computing, Networking and Security*, Mangalore, India, pp. 56-61, 2013. [CrossRef] [Google Scholar] [Publisher Link]

[20] J. Mohan, V. Krishnaveni, and Yanhui Guo, "MRI Denoising Using Nonlocal Neutrosophic Set Approach of Wiener Filtering," *Biomedical Signal Processing and Control*, vol. 8, no. 6, pp. 779-791, 2013. [CrossRef] [Google Scholar] [Publisher Link]

[21] Hosein M. Golshan, Reza P.R. Hasanzadeh, and Shahrokh C. Yousefzadeh, "An MRI Denoising Method Using Image Data Redundancy and Local SNR Estimation," *Magnetic Resonance Imaging*, vol. 31, no. 7, pp. 1206-1217, 2013. [CrossRef] [Google Scholar] [Publisher Link]

[22] Sudipto Dolui et al., "A New Similarity Measure for Non-Local Means Filtering of MRI Images," *Journal of Visual Communication and Image Representation*, vol. 24, no. 7, pp. 1040-1054, 2013. [CrossRef] [Google Scholar] [Publisher Link]

[23] Jeny Rajan, Arnold J. den Dekker, and Jan Sijbers, "A New Non-Local Maximum Likelihood Estimation Method for Rician Noise Reduction in Magnetic Resonance Images Using the Kolmogorov–Smirnov Test," *Signal Processing*, vol. 103, pp. 16-23, 2014. [CrossRef] [Google Scholar] [Publisher Link]

[24] S. Gopinathan, Radhakrishnan Kokila, and P. Thangavel, "Wavelet and FFT Based Image Denoising Using Non-linear Filters," *International Journal of Electrical and Computer Engineering*, vol. 5, no. 5, pp. 1018-1026, 2015. [CrossRef] [Google Scholar] [Publisher Link]

[25] Jian Yang et al., "Brain MR Image Denoising for Rician Noise Using Pre-Smooth Non-Local Means Filter," *BioMedical Engineering OnLine*, vol. 14, pp. 1-20, 2015. [CrossRef] [Google Scholar] [Publisher Link]

[26] Sidheswar Routray, Arun Kumar Ray, and Chandrabhanu Mishra, "MRI Denoising Using Sparse Based Curvelet Transform with Variance Stabilizing Transformation Framework," *Indonesian Journal of Electrical Engineering and Computer Science*, vol. 7, no. 1, pp. 116-122, 2017. [CrossRef] [Google Scholar] [Publisher Link]

[27] Herng-Hua Chang, Cheng-Yuan Li, and Audrey Haihong Gallogly, "Brain MR Image Restoration Using an Automatic Trilateral Filter With GPU-Based Acceleration," *IEEE Transactions on Biomedical Engineering*, vol. 65, no. 2, pp. 400-413, 2018. [CrossRef] [Google Scholar] [Publisher Link]